

Experimental investigation of quantum discord in spin-orbit X statesV. S. Lamego ^{1,2} D. G. Braga ^{1,2} W. F. Balthazar ^{2,3} and J. A. O. Huguenin ^{1,2,*}¹*Programa de Pós-graduação em Física, Instituto de Física, Universidade Federal Fluminense, Avenida General Milton Tavares de Souza s/n, Gragoatá, 24210-346 Niterói, Rio de Janeiro, Brazil*²*Instituto de Ciências Exatas, Universidade Federal Fluminense, 27213-145 Volta Redonda, Rio de Janeiro, Brazil*³*Instituto Federal do Rio de Janeiro, 27213-100 Volta Redonda, Rio de Janeiro, Brazil*

(Received 29 December 2023; accepted 9 August 2024; published 3 September 2024)

We perform an experimental study of quantum discord on spin-orbit modes of an intense laser beam, analogous to different X states. These modes are prepared through the incoherent superposition of different intense laser beams, encoding a two-qubit system in both polarization and the first-order Hermite-Gaussian modes [as proposed in *Phys. Rev. A* **103**, 022411 (2021)]. We characterize these modes by using all-optical tomography and calculated entropic quantum discord. Remarkably, even for high-fidelity mode reconstruction, the computation of quantum discord showed significant deviations from theoretical expectations. Then, we proposed a simple model based on noisy measurements that showed a small degradation of the fidelity of the output modes, giving rise to the strong deviation of the discord. Our results, both experimental data and the theoretical predictions, demonstrate good agreement.

DOI: [10.1103/PhysRevA.110.032601](https://doi.org/10.1103/PhysRevA.110.032601)**I. INTRODUCTION**

Quantum discord (QD) [1] is an important resource for quantum computation and quantum information [2], exploring a diverse range of scenarios where the relation of classical correlations and quantum mutual information is pivotal. These scenarios include applications such as remote-state preparation for quantum communication [3,4], critical systems [5], mixed-state metrology [6], spin models [7], and multiqubit systems [8]. In the QD dynamics scenario, investigations have been conducted on two-qubit systems in non-Markovian scenarios [9,10], as well as in the context of photonic crystals [11] and two-photon states [12].

Recently, QD has been an essential tool for different quantum tasks, such as quantum key distribution protocols [13,14] and quantum metrology [15]. Studies of correlations such as contextuality [16] and coherence, entanglement, and QD relation of X states [17] were developed. Such correlations lead to exploring quantum thermodynamics [18].

Considering some cases of mixed states for a given amount of classical correlation, it is important to maximize QD. This task was achieved using an unbalanced Bell state, giving rise to the maximally discordant mixed state (MDMS) [19]. Such states were generated by using dissipative schemes [20]. Two separable qubits presented QD quantified by local operations [21]. Lately, necessary conditions were demonstrated for obtaining maximally discordant, separable two-qubit X states [22]. The X states scenario is, indeed, a fertile environment for QD studies [23–25].

The use of structured light stands between the main platforms for implementing protocols and studies on quantum information and quantum computation. By associating the

polarization degree of freedom (DoF) and first-order transverse mode, we can prepare the well-known spin-orbit (SO) mode [26]. The quantum-classical analogy, presented by a laser beam prepared in nonseparable spin-orbit modes, has been investigated in experiments that showed violation of Bell inequality, pointing out the similar structure of nonseparable SO modes with entangled states [27–29]. By adding the path DoF, a tripartitelike state was prepared, and it was an observed violation of Mermin's inequalities [30]. These SO modes have also been used to study other correlations, such as contextuality [31]. Genuine entanglement between different DoF of a single photon emerges from quantization of SO modes [32].

Similarly, this platform has been employed to emulate various quantum information and quantum computation protocols, including quantum key distribution without referential frame [33], teleport protocol between DoF of light [34], and quantum channels [35]. Fundamental aspects have been explored as environment-induced entanglement [36] and non-Markovian signatures [37]. A seminal contribution was made through the optical simulation of quantum thermal machines [38]. We cannot forget the various implementations of logic gates exploiting structured light [39–41].

The study of QD presented in this paper is grounded in X state preparation using SO modes [42]. Different state preparation optical circuits were proposed for various states, including Werner states and other incoherent superpositions. A linear optical circuit for tomography of spin-orbit DoF was introduced. The preparation and characterization were computationally performed, and the calculated QD exhibited a remarkable agreement with theoretical expectations. Maximally discordant mixed states were proposed [43], necessitating the preparation of an unbalanced nonseparable mode, recently achieved experimentally [44]. However, to the best of our knowledge, no experimental studies on the quantum discord of spin-orbit X states have been performed.

*Contact author: jose_huguenin@id.uff.br

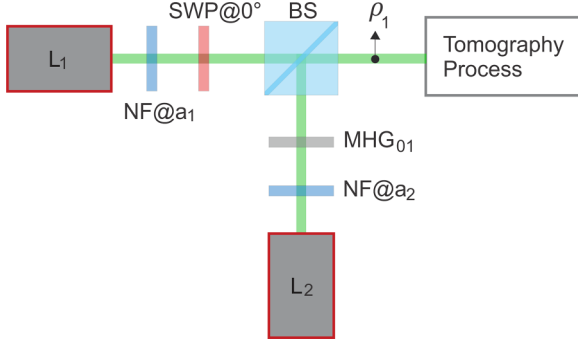


FIG. 1. Experimental setup to generate $\rho_1 = [(c/2, 0, 0, c/2); (0, 0, 0, 0); (0, 0, 0, 0); (c/2, 0, 0, 1 - c/2)]$. L_i ($i = 1, 2$) stands for lasers. M_{HG} stands for the holographic mask. NF stands for the variable neutral filter. BS stands for beam splitter. SWP stands for S-wave plate.

In this work we perform an experimental study of QD of spin-orbit modes of an intense laser beam analogous to different spin-orbit X state classes. We perform spin-orbit tomography. The effect of a nonfaithful reconstruction of those of the states in QD is investigated. The paper is organized as follows. In Sec. II we present a theoretical review, present QD calculation, and investigate spin-orbit modes. Section III presents the optical circuits for spin-orbit X states preparation and for performing spin-orbit tomography. The experimental results are presented and discussed in Sec. IV. Section V presents a model to study QD behavior, considering fidelity degradation induced by experimental errors. This study is necessary to understand our results. Finally, concluding remarks are presented in Sec. VI.

II. THEORETICAL REVIEW

A. Quantum discord

QD [1] is widely discussed in the literature, having applications in the development of quantum technologies and the study of the fundamentals of quantum mechanics. In technological contexts, QD serves as a quantum resource, enabling the exploration of quantum processing capabilities necessary

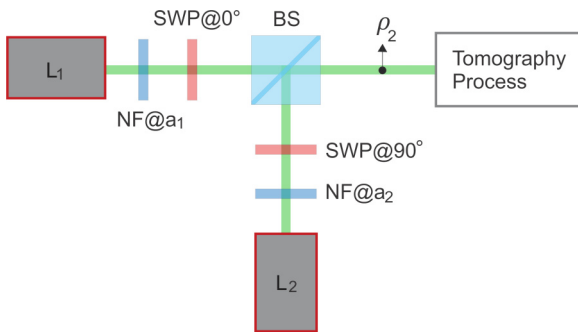


FIG. 2. Experimental setup to generate $\rho_2 = [(c/2, 0, 0, c/2); (0, (1 - c)/2, (c - 1)/2, 0); (0, (c - 1)/2, (1 - c)/2, 0); (c/2, 0, 0, c/2)]$. L_i ($i = 1, 2$) stands for lasers. PBS stands for polarized beam splitter. BS stands for beam splitter. HWP stands for half wave plate. SWP stands for S-wave plate.

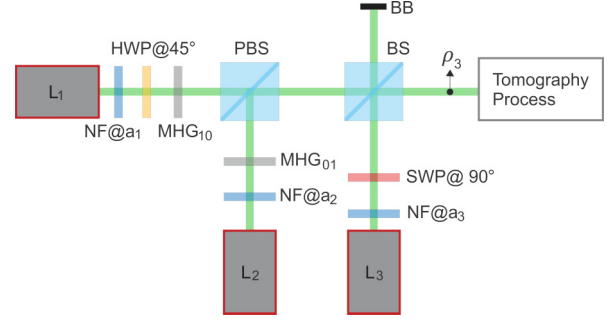


FIG. 3. Experimental setup to generate $\rho_3 = [((1 - c)/3, 0, 0, 0); (0, 1/3, -1/3, 0); (0, -1/3, 1/3, 0); (0, 0, 0, c/3)]$. L_i ($i = 1, 2, 3$) stands for lasers. M_{HG} stands for holographic mask. NF stands for the variable neutral filter. BS stands for beam splitter. SWP stands for S-wave plate. BB stands for beam block.

to achieve advantages in specific tasks [3,45,46]. Moreover, quantum discord (QD) is interpreted as an indicator of the system's quantum nature, effectively distinguishing between quantum and classical correlations [5,47]. Due to the complexity of the quantum realm, there are numerous definitions of quantum discord, including entropic QD and geometric QD [48].

For instance, for a bipartite system described as a density operator ρ_{AB} , the entropic QD is defined as

$$\mathcal{Q}(\rho_{AB}) := \mathcal{I}(\rho_{AB}) - \mathcal{C}_C(\rho_{AB}), \quad (1)$$

where $\mathcal{I}(\rho_{AB})$ is the usual quantum mutual information, and $\mathcal{C}_C(\rho_{AB})$ is the classical correlation given by

$$\mathcal{C}_C(\rho_{AB}) = \mathcal{S}(\rho_A) - \min_{\{B_i\}} \sum_i \mathcal{S}(\rho_{A|B_i}), \quad (2)$$

with $\mathcal{S}(\rho_A)$ and $\mathcal{S}(\rho_{A|B_i})$ the von Neumann entropy of subsystem A before and after performing a local measurement B_i on subsystem B, respectively. So the term $\mathcal{S}(\rho_{A|B_i})$ is interpreted as a measurement-induced conditional entropy which, for a two-qubit system, can be expressed as

$$\mathcal{S}(\rho_{A|B_i}) = p_0 \mathcal{S}(\rho_0) + p_1 \mathcal{S}(\rho_1). \quad (3)$$

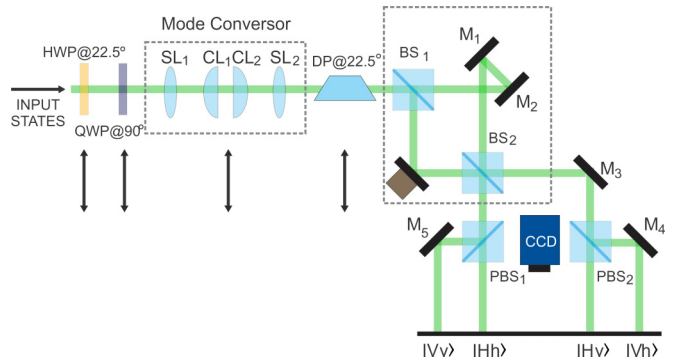


FIG. 4. Experimental setup to perform tomography. CL stands for cylindrical lenses. DP stands for Dove prism. HWP stands for half-wave plate. QWP stands for quarter-wave plate. MZIM stands for Mach-Zehnder interferometer with one additional mirror. M stands for mirror. PZT stands for mirror with a piezoelectric ceramic. PBS stands for polarized beam splitter. BS stands for beam splitter.

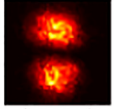
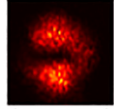
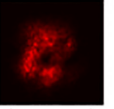
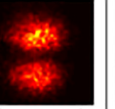
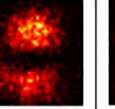
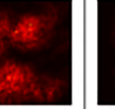
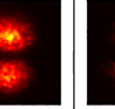
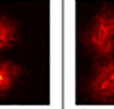
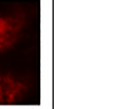



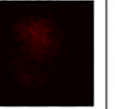
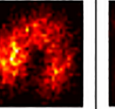
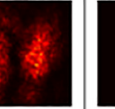
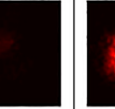
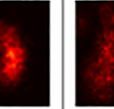
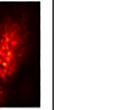

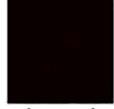
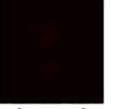
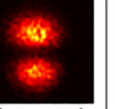
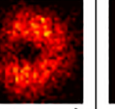
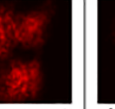
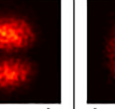
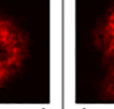
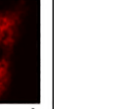
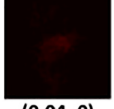
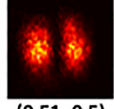
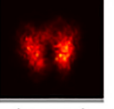
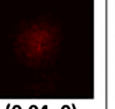
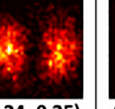
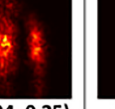
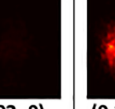
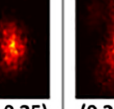
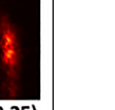
I_{Vv}	I_{Va}	I_{Vl}	I_{Av}	I_{Aa}	I_{Al}	I_{Lv}	I_{La}	I_{Ll}
 (0.96, 1)	 (0.48, 0.50)	 (0.47, 0.5)	 (0.52, 0.5)	 (0.23, 0.25)	 (0.28, 0.25)	 (0.52, 0.5)	 (0.21, 0.25)	 (0.29, 0.25)
I_{Hh}	I_{Hd}	I_{Hr}	I_{Dh}	I_{Dd}	I_{Dr}	I_{Rh}	I_{Rd}	I_{Rr}
 (0.00, 0)	 (0.01, 0.00)	 (0.01, 0)	 (0.03, 0)	 (0.27, 0.25)	 (0.28, 0.25)	 (0.03, 0)	 (0.28, 0.25)	 (0.26, 0.25)
I_{Hv}	I_{Ha}	I_{Hl}	I_{Dv}	I_{Da}	I_{Dl}	I_{Rv}	I_{Ra}	I_{Rl}
 (0.00, 0)	 (0.01, 0)	 (0.02, 0)	 (0.46, 0.5)	 (0.26, 0.25)	 (0.20, 0.25)	 (0.43, 0.5)	 (0.25, 0.25)	 (0.21, 0.25)
I_{Vh}	I_{Vd}	I_{Vr}	I_{Ah}	I_{Ad}	I_{Ar}	I_{Lh}	I_{Ld}	I_{Lr}
 (0.04, 0)	 (0.51, 0.5)	 (0.5, 0.5)	 (0.04, 0)	 (0.24, 0.25)	 (0.24, 0.25)	 (0.02, 0)	 (0.26, 0.25)	 (0.24, 0.25)

FIG. 5. Recorded images (false color) for ρ_1 in the case $c = 0$, corresponding to the separable mode $|Vv\rangle$ for tomographic measurements. Within the parenthesis, we provide the experimental (I_{exp}) and the theoretical (I_{theo}) normalized intensities. The pair ($I_{\text{exp}}, I_{\text{theo}}$) corresponds to experimental and theoretical normalized values, respectively, for the correspondent basis element.

Note that p_0 and p_1 are the probabilities of finding system A at the states ρ_0 and ρ_1 after performing a local von Neumann measurement $\{B_i\}$ on subsystem B. Equation (2) illustrates the necessity of a minimization procedure over all sets of von Neumann measurement operators $\{B_i\}$, which can be prohibitively hard to solve analytically, and for this reason, a general formula for two-qubit quantum discord is lacking. Despite this limitation, our work focuses on studying QD in the context of two-qubit X states, a well-known class of states for which a QD formula was derived in Ref. [24]. However, due to experimental errors in the state tomography process, the reconstructed state will not have an exact X form, invalidating the use of such formulas. Consequently, employing numerical methods to estimate QD is ultimately necessary. In this approach, classical correlation is obtained by numerically searching for the set of von Neumann measurements that maximizes the quantity given by Eq. (2). For this reason, precise knowledge of the system's density operator is critical for QD computation.

Even considering other approaches aimed at minimizing the measurement process, particularly in the context of geometric-based QD estimation [49], it remains necessary to

employ a complete tomography process for estimating entropic QD. For instance, in Ref. [50], a proposal is presented for obtaining QD through an alternative method, which involves the explicit measurement of system B on an optimal basis followed by a tomography process on subsystem A. The optimal basis is defined as the one that maximizes the quantity expressed by Eq. (2). Following Eq. (2), we can perform tomography on the reduced subsystem A before and after the local measurement on B, allowing us to compute the von Neumann entropy and subsequently estimate the classical correlation. However, it is important to note that even in this alternative approach, knowledge of the total density matrix remains indispensable once quantum mutual information depends on it.

B. Studied mixed spin-orbit X states

Spin-orbit modes can be understood as an integrated description of the electromagnetic field by polarization and transverse-mode DoF [26]. The most general SO modes are linear polarization \hat{e} and first-order Hermite-Gaussian (HG)

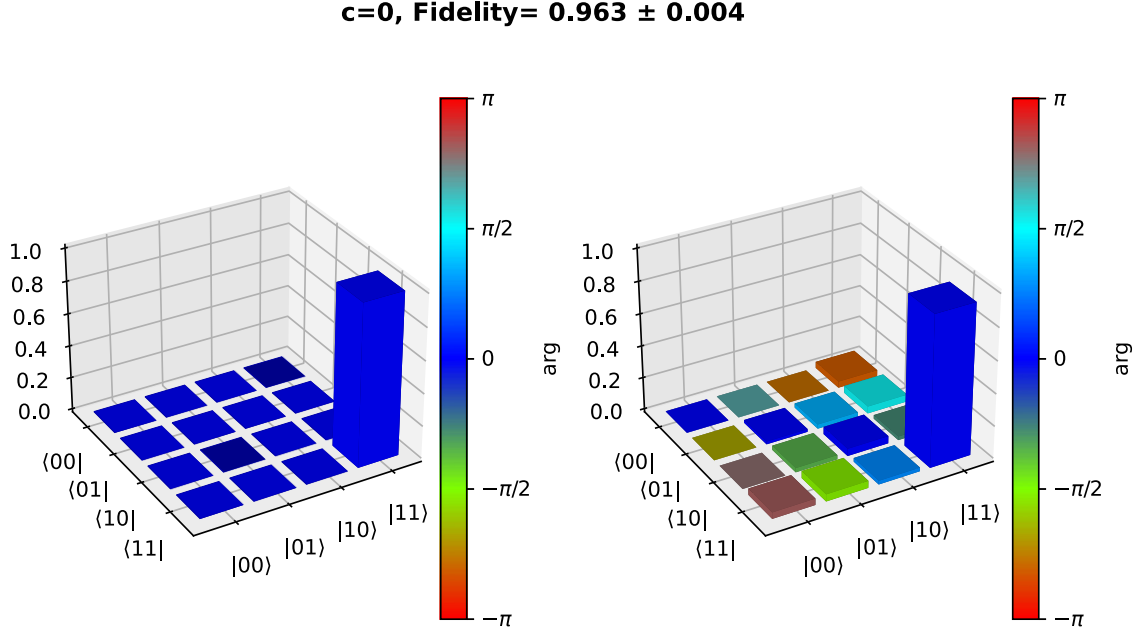


FIG. 6. Theoretical (left) and experimental (right) density matrix for the mode ρ_1 in the case $c = 0$ corresponding to the separable mode $|Vv\rangle$. The experimental result led us to $\rho_1 = [(0 + 0i, 0 + 0i, 0 + 0i, -0.03 - 0.02i); (0 + 0i, 0 + 0i, 0.02 - 0.03i, 0 + 0.05i); (0 + 0i, 0.02 - 0.03i, 0.04 + 0i, 0.02 - 0.02i); (-0.03 + 0.02i, 0 - 0.05i, 0.02 + 0.02i, 0.96 + 0i)]$. Fidelity of the reconstructed mode is $F = 0.963 \pm 0.004$.

modes, which can be written as

$$\begin{aligned} \vec{E}_{SO}(\vec{r}) = & \alpha \text{HG}_{10}(x, y) \hat{e}_H + \beta \text{HG}_{10}(x, y) \hat{e}_V \\ & + \gamma \text{HG}_{01}(x, y) \hat{e}_H + \delta \text{HG}_{01}(x, y) \hat{e}_V, \end{aligned} \quad (4)$$

where the Greek coefficients are complex numbers that obey the relation $|\alpha|^2 + |\beta|^2 + |\gamma|^2 + |\delta|^2 = 1$. When such a base is used for the quantization of the electromagnetic field, we can write the quantum state of the electromagnetic field as

$$\begin{aligned} |\psi_{SO}\rangle = & a_{Hh} |Hh\rangle + a_{Hv} |Hv\rangle + a_{vh} |Vh\rangle \\ & + a_{vv} |Vv\rangle, \end{aligned} \quad (5)$$

where we used the notation $\hat{e}_H \equiv H$, $\hat{e}_V \equiv V$ for polarization DoF, and $\text{HG}_{01}(\vec{r}) \equiv h$, $\text{HG}_{10}(\vec{r}) \equiv v$ for transverse-mode DoF. The probabilities amplitudes a_{ij} ($i = H, V$, $j = h, v$) are normalized.

Following the proposal of Ref. [42], the emulation of quantum mixed states can be accomplished by combining independent laser beams, with each beam encoding a pure state of two qubits. Once the lasers are independent, there is no well-defined phase relation between them and they do not interfere. So the measurement outcomes will be the sum of the contribution of intensity of each beam, providing the statistics of a mixed state.

The mixed modes experimentally investigated are the following:

$$\rho_1 = c |\phi^+\rangle \langle \phi^+| + (1 - c) |Vv\rangle \langle Vv|, \quad (6)$$

$$\rho_2 = c |\phi^+\rangle \langle \phi^+| + (1 - c) |\psi^-\rangle \langle \psi^-|, \quad (7)$$

$$\rho_3 = \frac{1}{3} [c |Vv\rangle \langle Vv| + (1 - c) |Hh\rangle \langle Hh| + 2 |\psi^-\rangle \langle \psi^-|], \quad (8)$$

where $c \in [0, 1]$. Here, $|\phi^+\rangle = \frac{1}{\sqrt{2}}(|Hh\rangle + |Vv\rangle)$ and $|\psi^-\rangle = \frac{1}{\sqrt{2}}(|Hv\rangle - |Vh\rangle)$ are the maximally nonseparable mode, analog of Bell states [27]. Once we need the density matrix to compute quantum discord, we must implement a two-qubit, quantumlike state tomography process to estimate the density matrix.

III. EXPERIMENT

A. State preparation

To prepare the states ρ_1 , ρ_2 , and ρ_3 , given, respectively, by Eqs. (6), (7), and (8), we use the circuits represented in Figs. 1–3, respectively. All those optical circuits operate similarly: we prepare ensembles of pure states encoded in independent beams, which are combined to produce a mixed state.

The optical circuit for preparing the state ρ_1 , given by Eq. (6), is shown in Fig. 1, illustrating an S-wave plate with the axis on angle $@0^\circ$ (SWP@ 0°) with the horizontal acts converting a vertically polarized input laser beam (L_1) into a maximally nonseparable spin-orbit mode $|\phi^+\rangle$. The neutral filter NF@ a_1 with adjustable transmittance (T_{a_1}) is used to control the intensity of mode $|\phi^+\rangle$.

On the other branch, an independently operated laser beam (L_2), vertically polarized, illuminates a holographic mask $M_{\text{HG}_{01}}$ to prepare the $\text{HG}_{01} \equiv v$ mode. The neutral filter NF@ a_2 with adjustable transmittance (T_{a_2}) is used to control the intensity of mode $|Vv\rangle$.

Both independent pure modes are superposed in a 50/50 beam splitter (BS) to produce mixed spin-orbit modes ρ_1 . By controlling the transmittance T_{a_1} and T_{a_2} of the neutral filters,

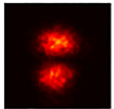
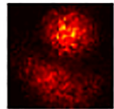
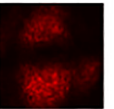
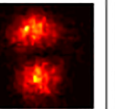
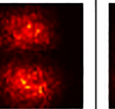
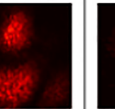
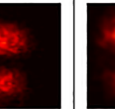
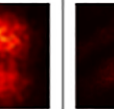
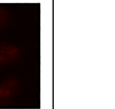
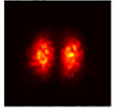
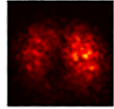
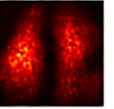
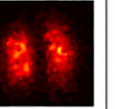
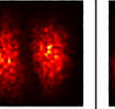
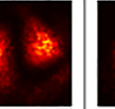
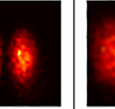
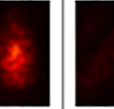
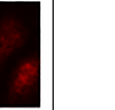
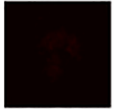
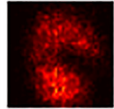
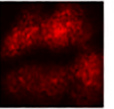
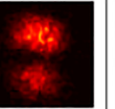
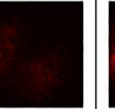
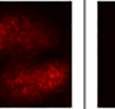
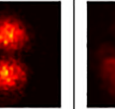
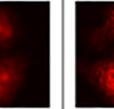
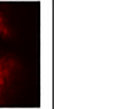
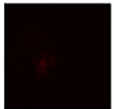
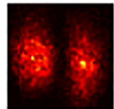
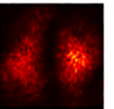
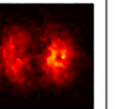
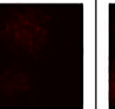
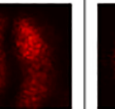
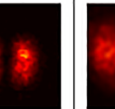
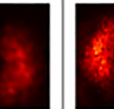
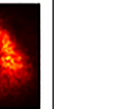
I_{Vv}	I_{Va}	I_{Vl}	I_{Av}	I_{Aa}	I_{Al}	I_{Lv}	I_{La}	I_{Ll}
 (0.47, 0.50)	 (0.26, 0.25)	 (0.30, 0.25)	 (0.27, 0.25)	 (0.44, 0.50)	 (0.30, 0.25)	 (0.21, 0.25)	 (0.26, 0.25)	 (0.08, 0.00)
I_{Hh}	I_{Hd}	I_{Hr}	I_{Dh}	I_{Dd}	I_{Dr}	I_{Rh}	I_{Rd}	I_{Rr}
 (0.49, 0.50)	 (0.20, 0.25)	 (0.24, 0.25)	 (0.26, 0.25)	 (0.45, 0.50)	 (0.24, 0.25)	 (0.31, 0.25)	 (0.24, 0.25)	 (0.10, 0.00)
I_{Hv}	I_{Ha}	I_{Hl}	I_{Dv}	I_{Da}	I_{Dl}	I_{Rv}	I_{Ra}	I_{Rl}
 (0.02, 0.00)	 (0.26, 0.25)	 (0.27, 0.25)	 (0.22, 0.25)	 (0.08, 0.00)	 (0.26, 0.25)	 (0.27, 0.25)	 (0.21, 0.25)	 (0.42, 0.50)
I_{Vh}	I_{Vd}	I_{Vr}	I_{Ah}	I_{Ad}	I_{Ar}	I_{Lh}	I_{Ld}	I_{Lr}
 (0.01, 0.00)	 (0.27, 0.25)	 (0.20, 0.25)	 (0.26, 0.25)	 (0.04, 0.00)	 (0.20, 0.25)	 (0.21, 0.25)	 (0.29, 0.25)	 (0.40, 0.50)

FIG. 7. Recorded images (false color) for maximally nonseparable state $|\phi^+\rangle$ tomographic measurements. Within the parenthesis, we provide the experimental (I_{exp}) the theoretical (I_{theo}), and normalized intensities. The pair $(I_{\text{exp}}, I_{\text{theo}})$ corresponds to experimental and theoretical normalized values, respectively, for the correspondent basis element.

the suit intensity proportions are adjusted to get the desired mixed state. To reproduce the mode class given by Eq. (6), we set $T_{a_1} = c$ and $T_{a_2} = 1 - c$.

For the ρ_2 mode, given by Eq. (7), the preparation requires the combination of two independent, maximally nonseparable modes, $|\phi^+\rangle$ and $|\psi^-\rangle$. Then, as shown in Fig. 2, a vertically polarized laser beam is directed through an S-wave plate (SWP@0°) to prepare the mode $|\phi^+\rangle$. The neutral filter NF@ a_1 controls the intensity using its transmittance T_{a_1} . A second vertically polarized laser (L2) has intensity controlled by the neutral filter NF@ a_2 with transmittance T_{a_2} , which is directed through a second S-wave plate at 90° (SWP@90°) to prepare the mode $|\psi^-\rangle$. A 50/50 BS is used superpose the mixed mode ρ_2 also by setting $T_{a_1} = c$ and $T_{a_2} = 1 - c$.

Finally, to prepare the mode ρ_3 given by Eq. (8), we used the optical circuit presented in Fig. 3. Note that the modes class ρ_3 is composed of a fixed fraction (2/3) of the maximally nonseparable mode $|\psi^-\rangle$, and the remaining 1/3 of the

intensity is composed by a variable convex combination of separable modes $|Hh\rangle$ and $|Vv\rangle$.

A laser (L1) then has its vertical polarization rotated 90° by the HWP@45°, and the MaskHG₁₀ produces the h HG mode that completes the $|Hh\rangle$ mode preparation. Its intensity is controlled by the neutral filter NF@ a_1 with transmittance T_{a_1} . A second laser (L2) prepares the mode $|Vv\rangle$ by using the MaskHG₀₁ and has its intensity controlled by the neutral filter NF@ a_2 with transmittance T_{a_2} . A third laser (L3) vertically polarized shines the SWP@90° to produce the maximally nonseparable mode $|\psi^-\rangle$, which has its intensity controlled by NF@ a_3 with transmittance T_{a_3} . The three modes are superposed in 50/50 BS, and the transmittances are adjusted as $T_{a_3} = 2/3$ of the total intensity, $T_{a_1} = c/3$ and $T_{a_2} = (1 - c)/3$.

The prepared state can be characterized by a tomography process, enabling us to reconstruct the state by accessing statistics obtained by a set of projective measurements on a different basis, as mentioned earlier.

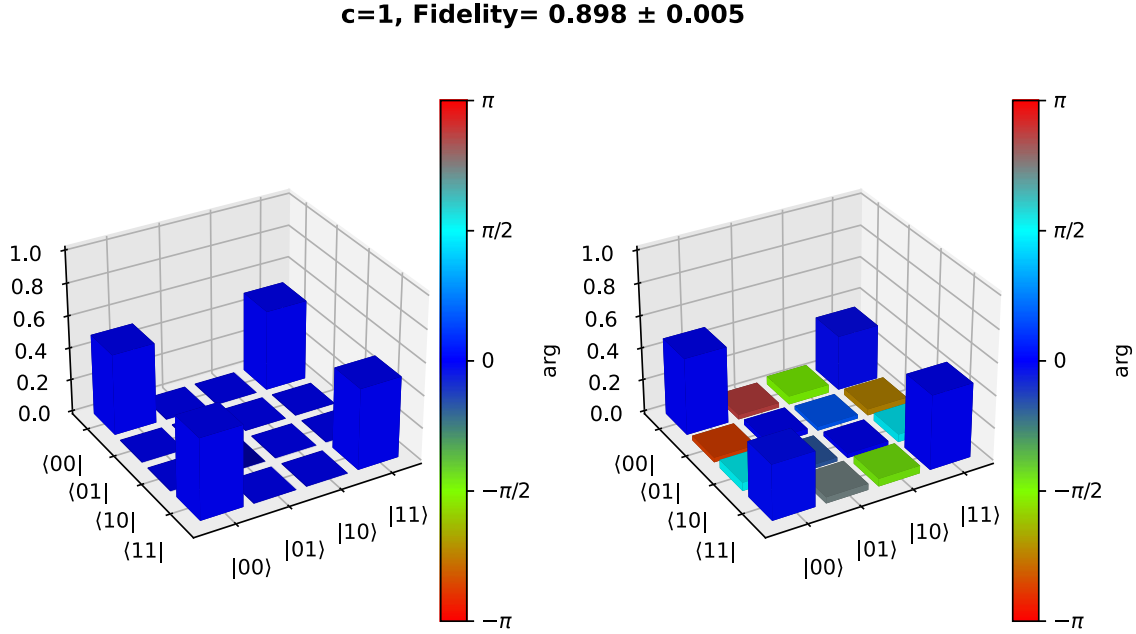


FIG. 8. Theoretical (left) and experimental (right) density matrix for ρ_1 in the case $c = 1$, corresponding to the maximally nonseparable mode $|\phi^+\rangle$. From the experimental result we have $\rho_1 = [(0.49 + 0i, -0.03 + 0.01i, 0 - 0.05i, 0.35 - 0.02i); (-0.03 - 0.01i, 0.02 + 0i, 0.03 + 0.02i, -0.03 - 0.03i); (0 + 0.05i, 0.03 - 0.02i, 0.01 + 0i, 0 + 0.05i); (0.35 + 0.02i, -0.03 + 0.03i, 0 - 0.05i, 0.47 + 0i)]$. The fidelity for reconstructed mode is $F = 0.898 \pm 0.005$.

B. Optical circuits for spin-orbit tomography

The spin-orbit mode tomography process can be implemented optically by the setup in Fig. 4, following [42]. This setup enables state reconstruction through a series of intensity measurements, which are used to calculate all Stokes parameters, S_{ij} [51], where $i, j = 0, 1, 2, 3$. The labels i and j are associated with polarization and transverse mode, respectively.

The MZIM (Mach-Zehnder interferometer with an additional mirror) associated with polarized beam splitters 1 and 2, PBS_1 and PBS_2 , measure the two-qubit computational basis $\{Hh, Hv, Vh, Vv\}$. The parity selection performed by the MZIM associated with PBSs gives us four intensity outputs I_{ij} related to the projections in each computational basis component. The outputs illuminate a screen that is captured by a monochromatic CCD camera. This setup provides an image recording the four intensities simultaneously, allowing us to calculate the probability of each basis component as follows:

$$P_{i,j} = \frac{I_{i,j}}{I_T}, \quad (9)$$

where $I_{i,j}$ ($i = H, V; j = h, v$) is the gray scale intensity integration of each component ij given by the image recorded by the CCD camera in the output ij . I_T is the total gray scale intensity obtained by the sum of the four outputs.

The measurement in the rotated basis of polarization DoF is performed by adding alternately in the input state path a half-wave plate at 22.5° (HWP@ 22.5°) and a quarter wave plate at 90° (QWP@ 90°). To measure the diagonal-antidiagonal (D/A) basis we include only the HWP@ 22.5° . For measurements in the right-left circular basis (R/L), we

used both HWP@ 22.5° and QWP.@ 90° associated with MZIM and PBS units.

For the d/a and r/l basis for transverse-mode DoF, a Dove prism with its base rotated by 22.5° plays an analog role of HWP@ 22.5° for h and v HG modes. The $\pi/2$ mode converter composed of two cylindrical lenses plays the role of QWP.@ 90° . It is worth mentioning that to satisfy the mode-matching requirement for the $\pi/2$ mode converter it is necessary to associate a pair of spherical lenses, denoted as SL_1 and SL_2 , as shown in Fig. 4. This is a sensitive point and a source of the most pronounced experimental error.

A detailed description of all tomographic measurement sets for each Stokes parameter for spin-orbit tomography can be found in the proposal of Ref. [42].

It is worth emphasizing the need for a set of lenses to control the laser waists, as we need to superimpose the modes of each independent laser to prepare the states. Most critically, for tomography, all modes must satisfy the mode-matching conditions of the cylindrical lens telescope and be aligned simultaneously in the MZIM. These lens assemblies are not shown in the experimental setups. Such control is fundamental for the measurement.

IV. EXPERIMENTAL RESULTS

In this section we present the experimental results for spin-orbit mixed-state tomography performed on the states theoretically described by Eqs. (6), (7), and (8).

A. Recovered spin-orbit mode density matrix

First, we present the results for the state ρ_1 . We will present the obtained images for $c = 0$, $c = 0.5$, and $c = 1$.

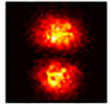
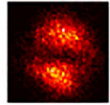
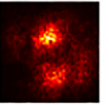
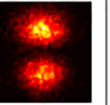
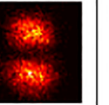
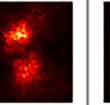
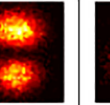
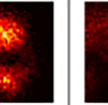
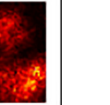
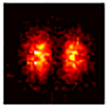
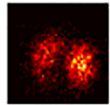
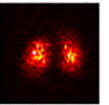
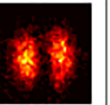
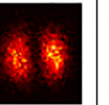
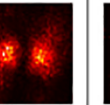
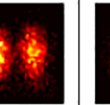
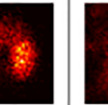
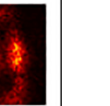
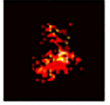
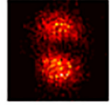
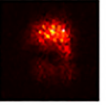
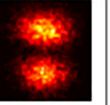
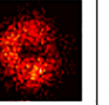
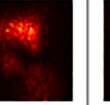
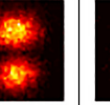
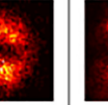
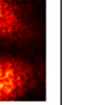

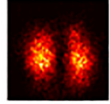
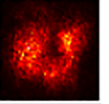
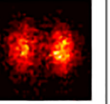
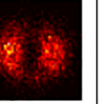
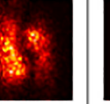
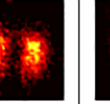
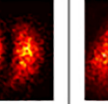
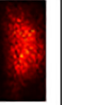
I_{Vv}	I_{Va}	I_{Vl}	I_{Av}	I_{Aa}	I_{Al}	I_{Lv}	I_{La}	I_{Ll}
 (0.66, 0.75)	 (0.36, 0.37)	 (0.39, 0.37)	 (0.38, 0.37)	 (0.37, 0.37)	 (0.30, 0.25)	 (0.39, 0.37)	 (0.23, 0.25)	 (0.16, 0.12)
I_{Hh}	I_{Hd}	I_{Hr}	I_{Dh}	I_{Dd}	I_{Dr}	I_{Rh}	I_{Rd}	I_{Rr}
 (0.28, 0.25)	 (0.11, 0.12)	 (0.13, 0.12)	 (0.12, 0.12)	 (0.32, 0.37)	 (0.25, 0.25)	 (0.15, 0.12)	 (0.26, 0.25)	 (0.15, 0.12)
I_{Hv}	I_{Ha}	I_{Hl}	I_{Dv}	I_{Da}	I_{Dl}	I_{Rv}	I_{Ra}	I_{Rl}
 (0.02, 0.00)	 (0.14, 0.12)	 (0.14, 0.12)	 (0.38, 0.37)	 (0.12, 0.12)	 (0.23, 0.25)	 (0.37, 0.37)	 (0.23, 0.25)	 (0.39, 0.37)
I_{Vh}	I_{Vd}	I_{Vr}	I_{Ah}	I_{Ad}	I_{Ar}	I_{Lh}	I_{Ld}	I_{Lr}
 (0.05, 0.00)	 (0.39, 0.37)	 (0.34, 0.37)	 (0.12, 0.12)	 (0.19, 0.12)	 (0.23, 0.25)	 (0.10, 0.12)	 (0.27, 0.25)	 (0.29, 0.37)

FIG. 9. Recorded images (false color) for ρ_1 in the case $c = 0.5$, corresponding to a balanced mixed mode for tomographic measurements. Within the parenthesis we provide the experimental (I_{exp}) and the theoretical (I_{theo}) normalized intensities. The pair ($I_{\text{exp}}, I_{\text{theo}}$) corresponds to experimental and theoretical normalized values, respectively, for the correspondent basis element.

Figure 5 presents the recorded images (false color) for the tomographic measurement for $c = 0$ that corresponds to the separable mode $|Vv\rangle$ for each set of basis. The image labeled as I_{Vv} is the intensity recorded in the output for the component $|Vv\rangle$, corresponding to the set of the computational basis for polarization $\{H, V\}$ and transverse mode $\{h, v\}$. The image labeled as I_{La} corresponds to measurement on a rotated basis, which is the intensity recorded in the output for the component $|La\rangle$, corresponding to the mode with left circular polarization ($|L\rangle$), corresponding to component L measured with a set of rotated basis right-left ($\{R, L\}$) for polarization and the transverse mode $|-\rangle$ corresponding to the component “ a ” of the measurement in the diagonal-antidiagonal basis $\{d, a\}$. Then, all labels indicate one result of the 36 combined measurements in the three bases for each DoF required for tomography [42].

The parenthesis below each image presents experimental and theoretical normalized intensities, in pairs ($I_{\text{exp}}, I_{\text{theo}}$), respectively, for the correspondent basis element. Although the values are generally close, certain deviations can be attributed to previously mentioned experimental errors. As the number of optical elements increases, deviations are ampli-

fied, as expected. Particularly, measurements on the basis set $\{Rr, Rl, Lr, Ll\}$ exhibit more deviations as it requires more optical elements. These measurements are notably affected by astigmatic optical devices such as the mode converter and the Dove prism complicating the alignment process and inserting aberrations in DoF. It is important to stress Dove prism slightly affects the polarization DoF. Consequently, some outputs that ideally should have no intensity are observed to be illuminated. This will impact the quantum state tomography process, leading to a decrease in fidelity.

Figure 6 presents the theoretical (left) and experimental (right) density matrix of the mode $c = 0$. As we can see, we obtained a good agreement with theoretical expectations. The fidelity of the reconstructed mode is $F = 0.963 \pm 0.004$. The error was estimated using Monte Carlo simulations, considering the uncertainty in intensity measurements. The same approach was used to calculate the errors of all experimental data. Mode $|Vv\rangle$ is not hard to prepare, and its fidelity would be closer to unity. This points out that the main question for fidelity in this case is not the mode preparation but the tomography process that requires astigmatic components. All these difficulties discussed above introduce noise in the

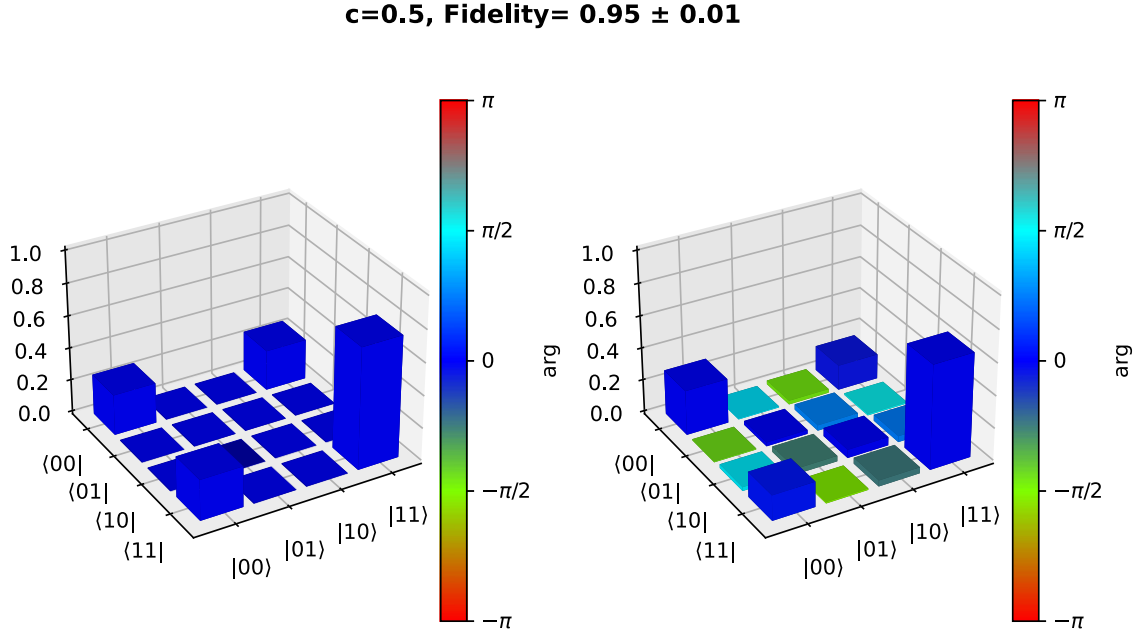


FIG. 10. Theoretical (left) and experimental (right) density matrix for ρ_1 in the case $c = 0.5$, corresponding to a balanced mixed mode given by Eq. (6). The experimental result give $\rho_1 = [(0.28 + 0i, -0.02 + 0.01i, 0 - 0.02i, 0.16 - 0.02i); (-0.02 - 0.01i, 0.02 + 0i, 0.03 + 0.03i, 0 + 0.01i); (0 + 0.02i, 0.03 - 0.03i, 0.05 + 0i, 0.01 + 0.03i); (0.16 + 0.02i, 0 - 0.01i, 0.01 - 0.03i, 0.66 + 0i)]$. The fidelity for the reconstructed mode is $F = 0.95 \pm 0.01$.

measurements and impose a limit on the fidelity of the reconstructed density matrix.

Let us present the results for the mode with $c = 1.00$, corresponding to the maximally nonseparable pure mode $|\phi^+\rangle$. Figure 7 presents the recorded image (false color) obtained for the tomographic measurement. The pair $(I_{\text{exp}}, I_{\text{theo}})$ corresponds to experimental and theoretical normalized values, respectively, for the correspondent basis element.

Theoretical (left) and experimental (right) density matrix for the mode ρ_1 with $c = 1$ ($|\phi^+\rangle$) is presented in Fig. 8. As shown, we observe good agreement between theory and experiment with fidelity $F = 0.897 \pm 0.005$. The mode $|\phi^+\rangle$ was prepared with an S-wave plate, which presents high conversion efficiency. We believe the limitation of the fidelity is due to tomographic measurements.

Let us present the results for ρ_1 in the case $c = 0.5$, which corresponds to a balanced mixed mode. Figure 9 presents the captured images. Note that we can identify the composition of the intensities shown in Figs. 5 and 7 images, once the intensities coming from each laser are added to the CCD. We verify an agreement between experimental results and theoretical expectations for normalized intensity as shown at the bottom of each image.

The obtained density matrix for ρ_1 , given by Eq. (6), for $c = 0.5$ is shown in Fig. 10. Theoretical (left) and experimental (right) results agree with fidelity 0.95 ± 0.01 . In the previous case, we have a decrease in the coherence terms and a variation in the phase, as explained above.

Let us show the obtained density matrix for the other two investigated mixed modes. Figure 11 shows the theoretical (left) and experimental (right) density matrix for the mode ρ_1 ,

given by Eq. (6), for $c = 0.25$ and $c = 0.75$. The results are in good agreement, and the fidelity is above 0.95.

Figure 12 shows the results for the density matrix of the mode ρ_2 , given by Eq. (7), for $c = 0.25$, $c = 0.5$, and $c = 0.75$. Good agreement between the experimental results (right) and the theoretical expectations (left) was observed, with fidelity around 0.90.

Finally, results for the density matrix of the mode ρ_3 [Eq. (8)] are presented in Fig. 13. Again, we can see a good agreement between the experimental results (right) and theoretical expectations (left) for $c = 0.25$, $c = 0.5$, and $c = 0.75$. Fidelity is higher than 0.90.

In our optical experimental setup (which involves preparation and tomography), several typical sources of error exist, including imperfections in optical elements, misalignment, and imperfect mode matching for the mode converter. Furthermore, the errors increase with the number of optical components required for a measurement. For example, the measurement in the y basis requires numerous optical elements, employing astigmatic optical elements such as the mode converter, significantly contributing to errors in density matrix estimation. Such experimental errors affect the fidelity of the reconstructed density matrix and, as we will see in the sequence, deeply affect the QD calculation.

B. Experimental quantum discord for spin-orbit modes

Once the density operator is obtained, the computation of QD can be performed numerically as explained in Sec. II A. Figure 14(a) presents the QD for the mode ρ_1 as a function of c . Experimental results are represented by the dots for $c = 0.0, 0.25, 0.5, 0.75$, and 1.0 , while the solid line

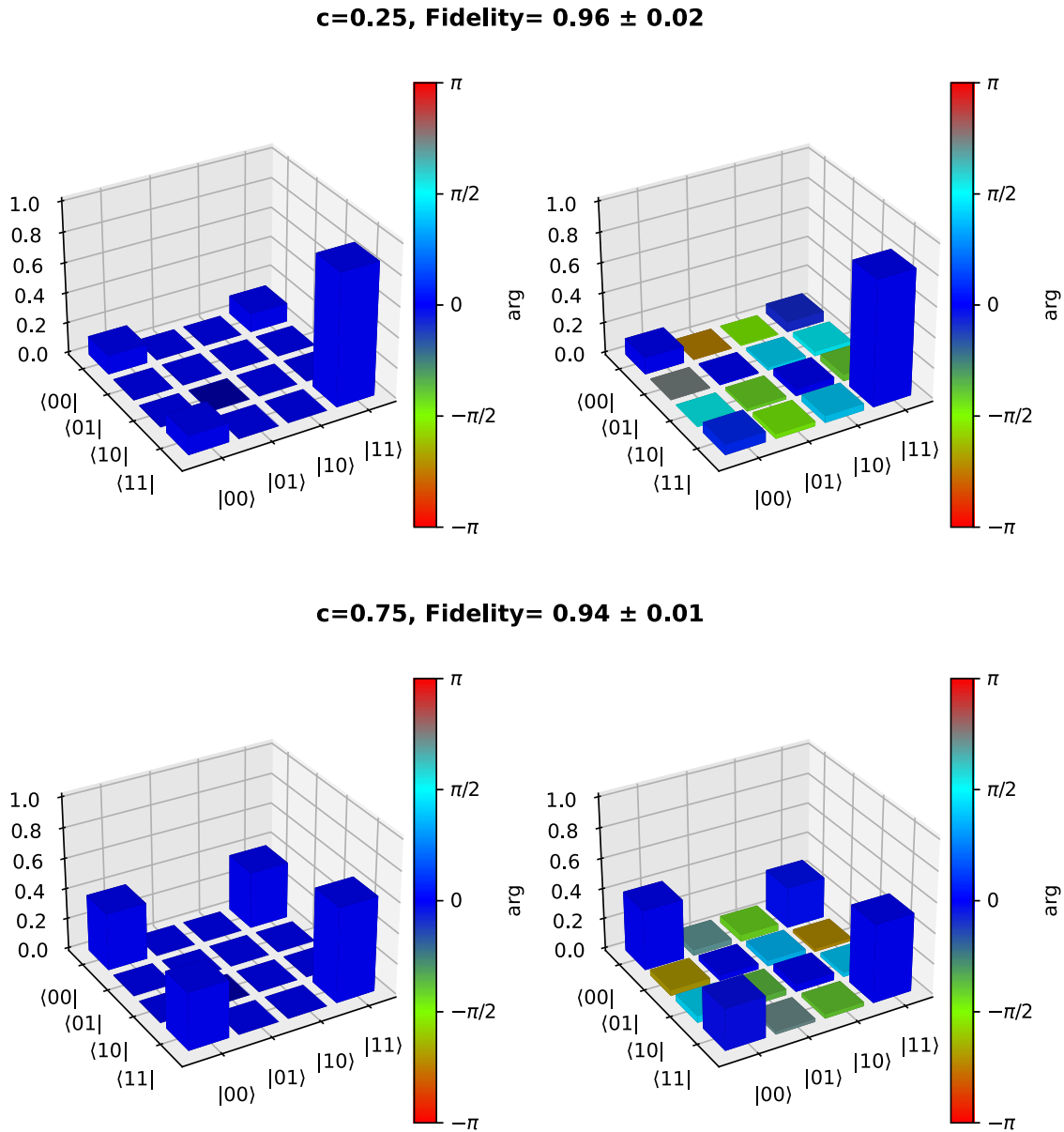


FIG. 11. Density matrices for state ρ_1 . For $c = 0.25$ we have $\rho_1 = [(0.11 + 0i, 0 + 0i, 0 - 0.01i, 0.07 - 0.02i); (0 + 0i, 0 + 0i, 0.01 + 0.02i, 0 + 0.03i); (0 + 0.01i, 0.01 - 0.02i, 0.05 + 0i, 0.01 - 0.04i); (0.07 + 0.02i, 0 - 0.03i, 0.01 + 0.04i, 0.84 + 0i)]$; and for $c = 0.75$, $\rho_1 = [(0.41 + 0i, -0.02 + 0.04i, 0.01 - 0.05i, 0.28 + 0.02i); (-0.02 - 0.04i, 0.02 + 0i, 0.02 + 0.05i, -0.01 - 0.02i); (0.01 + 0.05i, 0.02 - 0.05i, 0.04 + 0i, 0.01 + 0.03i); (0.28 - 0.02i, -0.01 + 0.02i, 0.01 - 0.03i, 0.53 + 0i)]$. The weights are represented in the top left side. The theoretical matrices are on the left side, while the experimental one is on the right.

represents the quantum theory prediction. The mean fidelity for the prepared modes of the class ρ_1 was $F = 0.95$. As we can see, the experimental results agree with theory until $c \approx 0.5$, and a disclosing is observed with experimental data varying less than theoretical prediction.

The same analysis can be performed for the class of modes ρ_2 , as shown in Fig. 14(b). The experimental results agree with the theoretical expectation for $0.2 < c < 0.8$. The mean fidelity for this class of states is $F = 0.90$. However, for $c \rightarrow 0$ and $c \rightarrow 1$, we also observe a noticeable discrepancy between theory and experiment, with a significant degradation of QD. By comparing with ρ_1 we realized that as the mode approaches a nonseparable spin-orbit mode

that is maximally coherent the experiment diverges from theory.

Finally, for ρ_3 , Fig. 14(c) shows the results for the class ρ_3 . Here we have the worst results compared with the theory. Even with a high mean fidelity ($F = 0.95$) we do not observe any intersection between theory and experiment. It is worth mentioning that such states present a fixed term proportional to Bell-like modes, which is maximally discordant and presents maximal coherence.

In the next section we discuss the degradation of QD even for modes with high fidelity and propose a simple model to explain the apparent mismatch between theory and experiment.

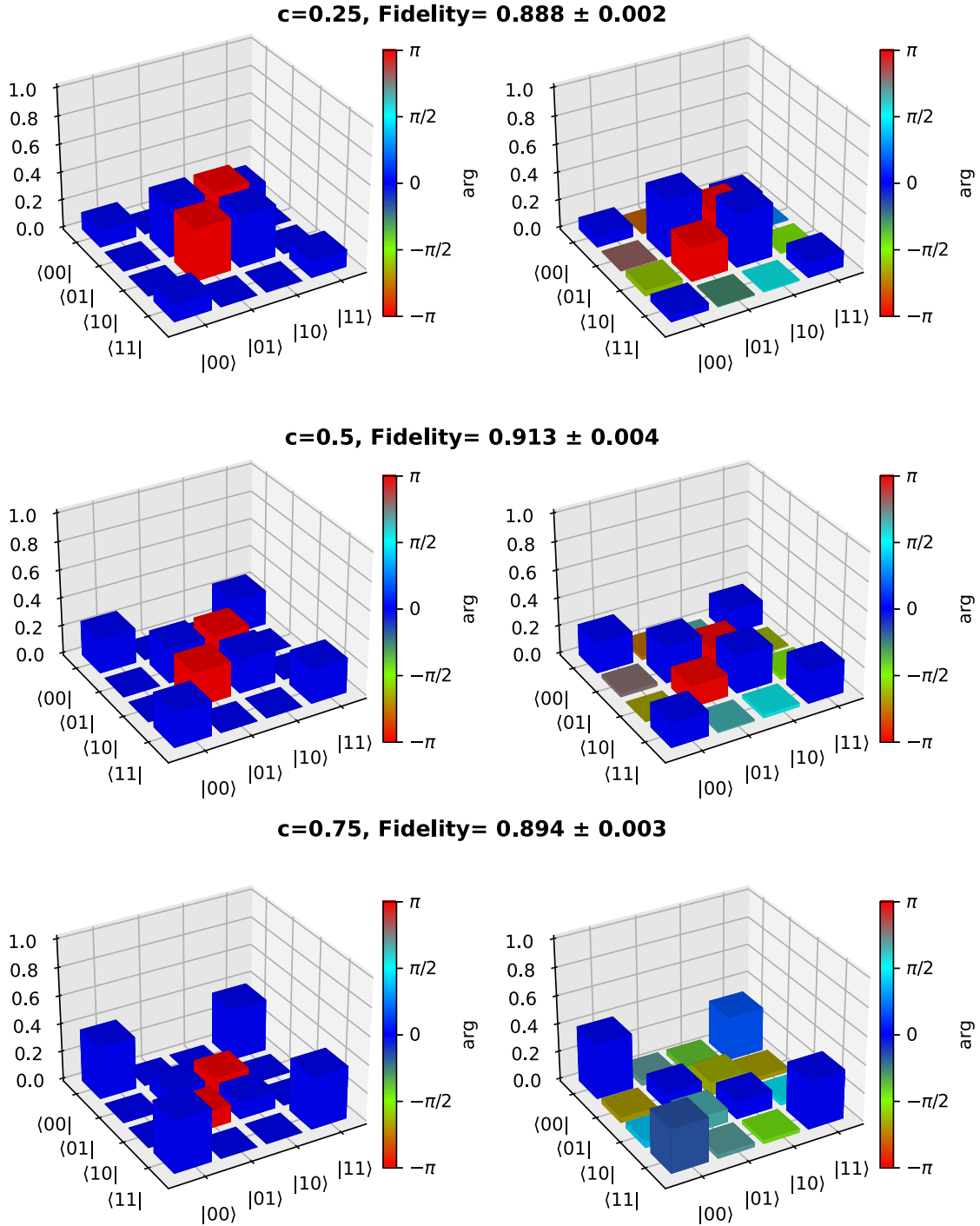


FIG. 12. Density matrices for state ρ_2 . For $c = 0.25$ we have $\rho_2 = [(0.09 + 0i, -0.01 - 0.01i, -0.01 + 0.04i, 0.05 - 0i); (-0.01 + 0.01i, 0.41 + 0i, -0.24 - 0i, 0.01 + 0.01i); (-0.01 - 0.04i, -0.24 + 0i, 0.39 + 0i, 0 - 0.01i); (0.05 + 0i, 0.01 - 0.01i, 0 + 0.01i, 0.11 + 0i)]$; for $c = 0.5$, $\rho_2 = [(0.23 + 0i, -0.02 - 0.02i, 0 + 0i, 0.18 - 0i); (-0.02 + 0.02i, 0.26 + 0i, -0.16 + 0.01i, 0 - 0.01i); (0 - 0i, -0.16 - 0.01i, 0.27 + 0i, 0 - 0.03i); (0.18 + 0i, 0 + 0.01i, 0 + 0.03i, 0.24 + 0i)]$, and for $c = 0.75$, $\rho_2 = [(0.4 + 0i, -0.02 + 0.03i, 0.01 - 0.04i, 0.27 + 0.16i); (-0.02 - 0.03i, 0.12 + 0i, -0.04 - 0.09i, -0.02 - 0.03i); (0.01 + 0.04i, -0.04 + 0.09i, 0.13 + 0i, 0 + 0.03i); (0.27 - 0.16i, -0.02 + 0.03i, 0 - 0.03i, 0.35 + 0i)]$. The weights and fidelity are represented at the top. The theoretical matrices histogram is on the left side, while the experimental one is on the right.

V. QUANTUM DISCORD DEGRADATION FOR HIGH-FIDELITY STATES

Taking into account the experimental errors during the realization of the experiment, we realized that astigmatic elements

cause us to have nonzero intensities in outputs where we expected zero intensity. Then, one potential model involves decoherence effects that result in the intended state as a combination of the considered density operator and a white noise

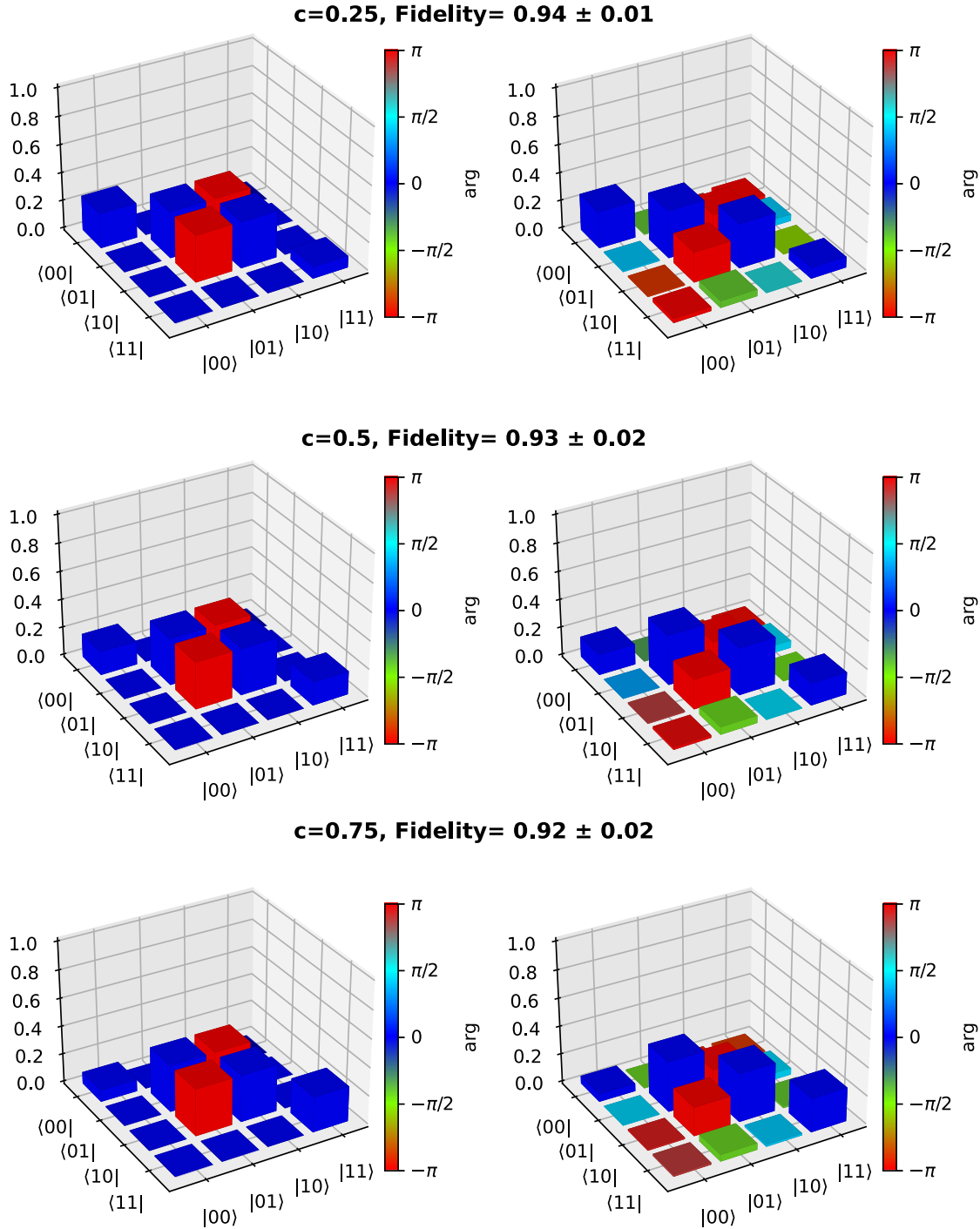


FIG. 13. Density matrices for state ρ_3 . For $c = 0.25$ we have $\rho_3 = [(0.26 + 0i, 0 - 0.01i, -0.01 + 0i, -0.02 - 0i); (0 + 0.01i, 0.34 + 0i, -0.22 + 0i, 0.02 + 0.05i); (-0.01 - 0i, -0.22 - 0i, 0.32 + 0i, 0 + 0i); (-0.02 + 0i, 0.02 - 0.05i, 0 + 0i, 0.08 + 0i)]$; for $c = 0.5$, $\rho_3 = [(0.15 + 0i, 0 + 0i, -0.01 + 0i, -0.02 + 0i); (0 + 0i, 0.36 + 0i, -0.21 + 0i, 0.01 + 0.05i); (-0.01 + 0i, -0.21 - 0i, 0.34 + 0i, 0 + 0i); (-0.02 + 0i, 0.01 - 0.05i, 0 + 0i, 0.16 + 0i)]$; and for $c = 0.75$, $\rho_3 = [(0.06 + 0i, 0 + 0i, -0.01 + 0i, -0.01 - 0.01i); (0 + 0i, 0.36 + 0i, -0.2 + 0.01i, 0.01 + 0.05i); (-0.01 + 0i, -0.2 - 0.01i, 0.35 + 0i, 0 - 0.01i); (-0.01 + 0.01i, 0.01 - 0.05i, 0 + 0.01i, 0.24 + 0i)]$. The weights are represented in the top. The theoretical matrices histogram are on the left side, while the experimental one is on the right.

term. Then, to study this effect, we insert an identity term with a controllable weight in states ρ_1 , ρ_2 , and ρ_3 . We have, therefore, a state perturbed ρ' defined as

$$\rho' = (1 - \alpha)\rho + \alpha I, \quad (10)$$

where α is the weight of the identity term. We used $\alpha = 0; 0.1; 0.2; 0.3$. This new noisy term will introduce a degradation of the fidelity of the prepared state and consequently, a degradation in the QD calculation.

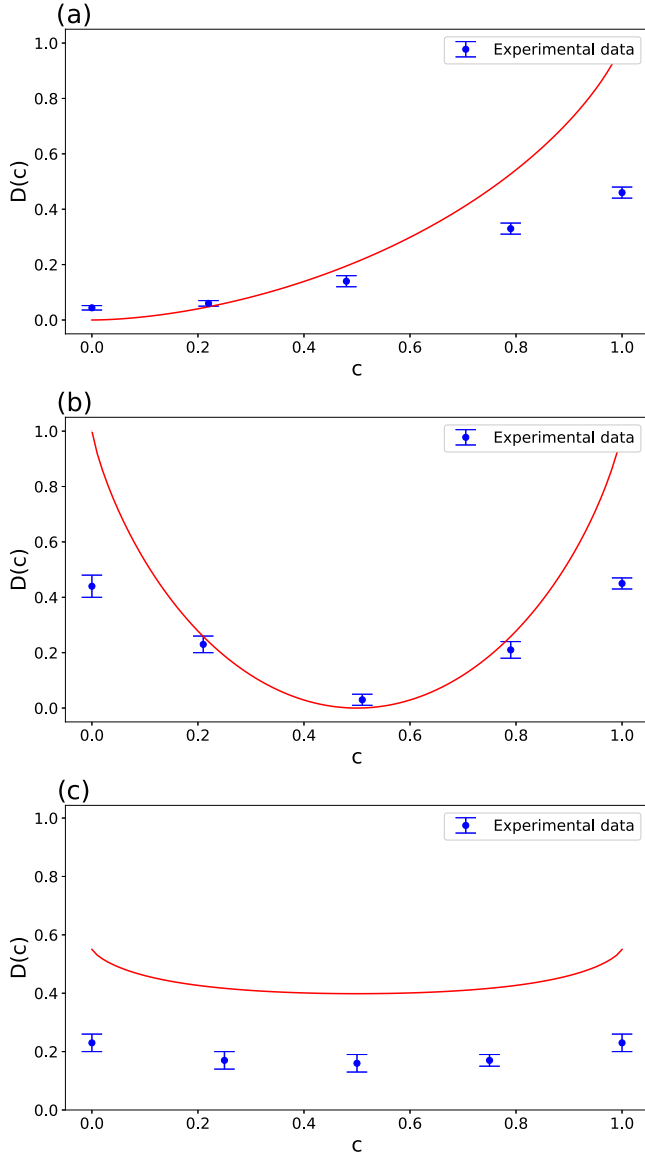


FIG. 14. Figures 14(a)–14(c) show graphs comparing the QD curves with experimental data (circles) for states ρ_1 , ρ_2 , and ρ_3 , respectively. The QD curve expected by quantum theory is shown by the solid line (red online).

Figure 15 presents the results for QD of ρ_1 . The theoretical expectation is observed for fidelity = 1.00 (solid line, red online). The mean fidelity F decreases as α increases, which leads to a sharp degradation of QD, as we can see for the studied cases of $F = 0.92$ ($\alpha = 0.1$, dotted line, blue online), $F = 0.85$ ($\alpha = 0.2$, dashed line, green online), and $F = 0.80$ ($\alpha = 0.4$, dashed-dotted line, black online). For $c > 0.1$, quantum discord (QD) degrades sharply as fidelity decreases. The QD of a pure Bell state ($c = 1$) shows more sensitivity to the loss of fidelity, where for a loss of $\approx 20\%$ in the fidelity we observed a degradation higher than 80% for QD.

Figure 16 presents the results for ρ_2 (mixing of two Bell-like modes). For $c = 0.5$, QD is null as expected, and the QD degrades fast for $c < 0.4$ and $c > 0.6$. As c approaches

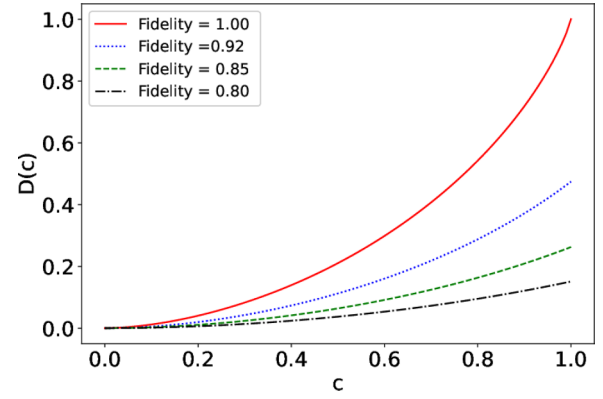


FIG. 15. QD in function of the weight c for state ρ_1 combined to identity. Mean fidelity = 1.00; 0.92; 0.85; 0.80 corresponds to $\alpha = 0$; 0.1; 0.2; 0.3, respectively.

0 or 1, QD degrades more deeply ($\approx 80\%$ for $\alpha = 0.3$) when fidelity also declines, however, with less intensity ($\approx 18\%$ for $\alpha = 0.3$). Again, pure Bell-like modes are more affected by noises.

Finally, for ρ_3 where we have a fixed term $\frac{2}{3} |\psi^-\rangle \langle \psi^-|$, which guarantees QD never vanishes, Fig. 17 shows we have a more degrading behavior of QD concerning fidelity. Note that for $F = 0.9$ QD partially vanishes independently of c 's values.

For the three modes studied, even with a high fidelity, an appreciable degradation of the QD is observed. The effect is more pronounced for coherent states. Such analysis helps us to interpret our experimental results. This model captures with good approximation the experimental data behavior.

Let us fit the experimental results with our model. For this purpose, for each class of states, we take the mean fidelity and use the curve of our model that corresponds to this mean fidelity. In Fig. 18(a) we show the fitting of experimental dots by the expected theoretical curve with fidelity $F = 0.95$, the mean fidelity obtained for ρ_1 . As can be seen, our results are consistent with the expected QD for the experimental mean fidelity. The fitting for ρ_2 is shown in Fig. 18(b) with the theoretical curve for the mean fidelity $F = 0.90$, also in good

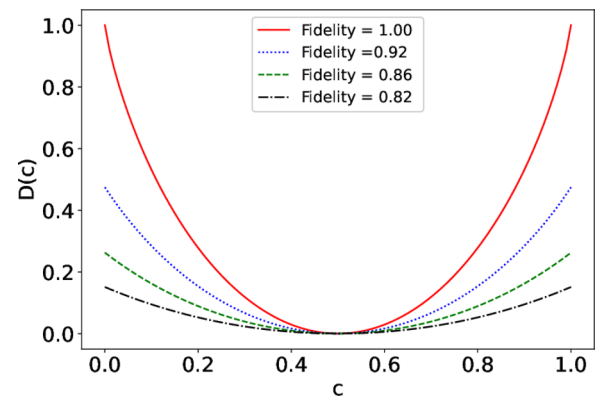


FIG. 16. QD as a function of the weight c for state ρ_2 combined to identity. Mean fidelity = 1.00; 0.92; 0.86; 0.82 corresponds to $\alpha = 0$; 0.1; 0.2; 0.3, respectively.

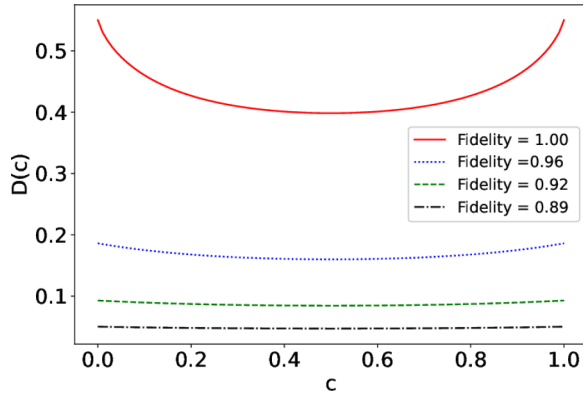


FIG. 17. Discord as a function of the weight c for state ρ_3 combined to identity. Mean fidelity = 1.00; 0.96; 0.92; 0.89 corresponds to $\alpha = 0; 0.1; 0.2; 0.3$, respectively.

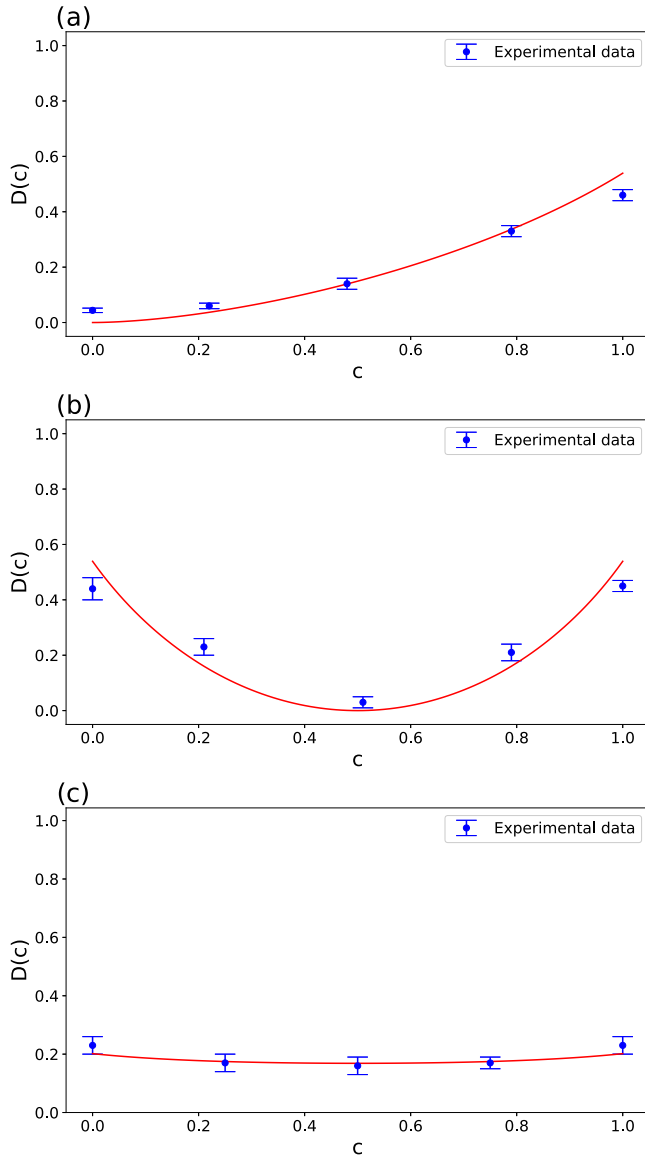


FIG. 18. QD fitting curve obtained for states ρ_1 , ρ_2 , and ρ_3 in this order from top to bottom. The fitting was done for ρ_1 , ρ_2 , and ρ_3 by considering the mean fidelity of 0.94, 0.95, and 0.95, respectively.

agreement with what is theoretically expected in our model. Finally, for ρ_3 [Fig. 18(c)], the more critical experimental divergence, the theory is consistent with the experiment.

This analysis allows us to visualize the effects caused by experimental errors that reduce fidelity and significantly impact the calculation of QD. It is important to emphasize that numerous steps in QD computation propagate errors into the final result. In this way, any small error on the density matrix is propagated on all those steps, resulting in the behavior observed. Consequently, even for a high level of fidelity we observed a substantial deviation in QD value as shown in the curves above.

VI. CONCLUSIONS

This work successfully demonstrates the experimental preparation and characterization of three distinct classes of mixed spin-orbit modes. We employed all-optical tomography to fully characterize these modes in both polarization and transverse-mode degrees of freedom. By reconstructing the density matrices of these X states, we were able to quantify their QD.

Considering the performed optical experiment, our circuit prepares and characterizes output measurements with high fidelity exceeding 90%, showing an outstanding performance. The primary source of errors is primarily attributed to the presence of the astigmatic elements that, unfortunately, distort the wavefront.

By comparing the experimental and theoretical QD, we observed a strong sensitivity of QD to experimental errors in the density matrix. This translates to a significant degradation of QD even for high-fidelity states. To address this, we have proposed a simple model to fit QD which is consistent with the theoretical predictions. This highlights the importance of considering the QD's sensitivity in future experimental designs and suggests the potential of our model for mitigating the impact of such errors in other research.

Our work yields noteworthy results by experimentally studying spin-orbit X states, an important platform for quantum information processing. Our findings not only shed light on the QD of these states but also delineate the crucial importance of overcoming limitations in experimental density matrix reconstruction, which is essential for measuring quantum correlations.

Finally, our model paves the way for further research and enhancements, including the strong sensitivity of entropic QD with fidelity, which can be explored in future theoretical research, expanding and generalizing our proposed model. Additionally, our findings highlight the demand for enhanced methods for performing measurements and unitary transformations, particularly in the transverse modes of spin-orbit modes. This capability is critical for fully exploration the potential of this platform in quantum information processing.

ACKNOWLEDGMENTS

We would like to thank the Brazilian funding agencies Conselho Nacional de Desenvolvimento Científico e Tecnológico (CNPq), Fundação Carlos Chagas Filho de Amparo à Pesquisa do Estado do Rio de Janeiro (FAPERJ),

Coordenação de Aperfeiçoamento de Pessoal de Nível Superior (CAPES) (Finance Code 001), and the Brazilian National

Institute for Science and Technology of Quantum Information (INCT-IQ) for financial support for this work.

-
- [1] H. Ollivier and W. H. Zurek, Quantum discord: A measure of the quantumness of correlations, *Phys. Rev. Lett.* **88**, 017901 (2001).
- [2] A. Brodutch, Discord and quantum computational resources, *Phys. Rev. A* **88**, 022307 (2013).
- [3] B. Dakic, Y. Lipp, X. Ma *et al.*, Quantum discord as resource for remote state preparation, *Nat. Phys.* **8**, 666 (2012).
- [4] V. Madhok and A. Datta, Quantum discord as a resource in quantum communication, *Int. J. Mod. Phys. B* **27**, 1345041 (2013).
- [5] M. S. Sarandy, Classical correlation and quantum discord in critical systems, *Phys. Rev. A* **80**, 022108 (2009).
- [6] K. Modi, H. Cable, M. Williamson, and V. Vedral, Quantum correlations in mixed-state metrology, *Phys. Rev. X* **1**, 021022 (2011).
- [7] Y. Huang, Scaling of quantum discord in spin models, *Phys. Rev. B* **89**, 054410 (2014).
- [8] B. Li, C.-L. Zhu, X.-B. Liang, B.-L. Ye, and S.-M. Fei, Quantum discord for multiqubit systems, *Phys. Rev. A* **104**, 012428 (2021).
- [9] F. F. Fanchini, T. Werlang, C. A. Brasil, L. G. E. Arruda, and A. O. Caldeira, Non-Markovian dynamics of quantum discord, *Phys. Rev. A* **81**, 052107 (2010).
- [10] S. Alipour, A. Mani, and A. T. Rezakhani, Quantum discord and non-Markovianity of quantum dynamics, *Phys. Rev. A* **85**, 052108 (2012).
- [11] J. Wang, H. Zhang, Y. Zhang, L. Zhang, T. Huang, S. Sun, and H.-Z. Zhang, Dynamics of quantum discord in photonic crystals, *Opt. Commun.* **285**, 2961 (2012).
- [12] K. Bartkiewicz, K. Lemr, A. Cernoch, and J. Soubusta, Measuring nonclassical correlations of two-photon states, *Phys. Rev. A* **87**, 062102 (2013).
- [13] R. Wang and C.-M. Zhang, Realizing fully reference-frame-independent quantum key distribution by exploiting quantum discord, [arXiv:2305.09404](https://arxiv.org/abs/2305.09404).
- [14] R. Wang, G.-J. Fan-Yuan, Z.-Q. Yin, S. Wang, H.-W. Li, Y. Yao, W. Chen, G.-C. Guo, and Z.-F. Han, Secure key from quantum discord, [arXiv:2304.05880](https://arxiv.org/abs/2304.05880).
- [15] A. Sone, Q. Zhuang, C. Li, Y. X. Liu, and P. Cappellaro, Nonclassical correlations for quantum metrology in thermal equilibrium, *Phys. Rev. A* **99**, 052318 (2019).
- [16] A. Al-Qasimi, Contextuality and quantum discord, *Phys. Lett. A* **449**, 128347 (2022).
- [17] J. D. Young and A. Auyuanet, Entanglement-coherence and discord—Coherence analytical relations for X states, *Quantum Inf. Proc.* **19**, 398 (2020).
- [18] Y. Xiao, D. Liu, J. He, Y. Ma, Z. Wu, and J. Wang, Quantum Otto engine with quantum correlations, *Phys. Rev. A* **108**, 042614 (2023).
- [19] F. Galve, G. L. Giorgi, and R. Zambrini, Maximally discordant mixed states of two qubits, *Phys. Rev. A* **83**, 012102 (2011).
- [20] X. X. Li, H. D. Yin, D. X. Li, and X. Q. Shao, Deterministic generation of maximally discordant mixed states by dissipation, *Phys. Rev. A* **101**, 012329 (2020).
- [21] S. Gharibian, Quantifying nonclassicality with local unitary operations, *Phys. Rev. A* **86**, 042106 (2012).
- [22] S. Rana and P. Parashar, Maximally discordant separable two-qubit states, *Quantum Inf. Proc.* **13**, 2815 (2014).
- [23] T. Yu and J. H. Eberly, Evolution from entanglement to decoherence of bipartite mixed X states, *Quantum Inf. Comput.* **7**, 459 (2007).
- [24] M. Ali, A. R. P. Rau, and G. Alber, Quantum discord for two-qubit X states, *Phys. Rev. A* **81**, 042105 (2010).
- [25] Q. Chen, C. Zhang, S. Yu, X. X. Yi, and C. H. Oh, Quantum discord of two-qubit X states, *Phys. Rev. A* **84**, 042313 (2011).
- [26] C. E. R. Souza, J. A. O. Huguenin, P. Milman, and A. Z. Khoury, Topological phase for spin-orbit transformations on a laser beam, *Phys. Rev. Lett.* **99**, 160401 (2007).
- [27] C. V. S. Borges, M. Hor-Meyll, J. A. O. Huguenin, and A. Z. Khoury, Bell-like inequality for the spin-orbit separability of a laser beam, *Phys. Rev. A* **82**, 033833 (2010).
- [28] K. H. Kagalwala, G. Di Giuseppe, A. F. Abouraddy, and B. E. A. Saleh, Bell's measure in classical optical coherence, *Nat. Photonics* **7**, 72 (2013).
- [29] X.-F. Qian, B. Little, J. C. Howell, and J. H. Eberly, Shifting the quantum-classical boundary: Theory and experiment for statistically classical optical fields, *Optica* **2**, 611 (2015).
- [30] W. F. Balthazar, C. E. R. Souza, D. P. Caetano, E. F. Galvão, J. A. O. Huguenin, and A. Z. Khoury, Tripartite nonseparability in classical optics, *Opt. Lett.* **41**, 5797 (2016).
- [31] M. H. Passos, W. F. Balthazar, J. A. Barros, C. E. R. Souza, A. Z. Khoury, and J. A. O. Huguenin, Classical analog of quantum contextuality in spin-orbit laser modes, *Phys. Rev. A* **98**, 062116 (2018).
- [32] L. J. Pereira, A. Z. Khoury, and K. Dechoum, Quantum and classical separability of spin-orbit laser modes, *Phys. Rev. A* **90**, 053842 (2014).
- [33] S. P. Walborn, D. S. Lemelle, M. P. Almeida, and P. H. Souto Ribeiro, Quantum key distribution with higher-order alphabets using spatially encoded qudits, *Phys. Rev. Lett.* **96**, 090501 (2006).
- [34] B. Pinheiro da Silva, M. Astigarreta Leal, C. E. R. Souza, E. F. Galvão, and A. Z. Khoury, Spin-orbit laser mode transfer via a classical analogue of quantum teleportation, *J. Phys. B: At. Mol. Opt. Phys.* **49**, 055501 (2016).
- [35] P. C. Obando, M. H. M. Passos, F. M. Paula, and J. A. O. Huguenin, Simulating Markovian quantum decoherence processes through an all-optical setup, *Quantum Inf. Proc.* **19**, 7 (2020).
- [36] M. H. M. Passos, W. F. Balthazar, A. Z. Khoury, M. Hor-Meyll, L. Davidovich, and J. A. O. Huguenin, Experimental investigation of environment-induced entanglement using an all-optical setup, *Phys. Rev. A* **97**, 022321 (2018).
- [37] M. H. M. Passos, P. C. Obando, W. F. Balthazar, F. M. Paula, J. A. O. Huguenin, and M. S. Sarandy, Non-Markovianity through quantum coherence in an alloptical setup, *Opt. Lett.* **44**, 2478 (2019).

- [38] M. H. M. Passos, A. C. Santos, M. S. Sarandy, and J. A. O. Huguenin, Optical simulation of a quantum thermal machine, *Phys. Rev. A* **100**, 022113 (2019).
- [39] W. F. Balthazar, D. P. Caetano, C. E. R. Souza, and J. A. O. Huguenin, Using polarization to control the phase of spatial modes for application in quantum information, *Braz. J. Phys.* **44**, 658 (2014).
- [40] W. F. Balthazar and J. A. O. Huguenin, Conditional operation using three degrees of freedom of a laser beam for application in quantum information, *J. Opt. Soc. Am. B* **33**, 1649 (2016).
- [41] L.-P. Deng, H. Wang, and K. Wang, Quantum CNOT gates with orbital angular momentum and polarization of single-photon quantum logic, *J. Opt. Soc. Am. B* **24**, 2517 (2007).
- [42] W. F. Balthazar, D. G. Braga, V. S. Lamego, M. M. M. Passos, and J. A. O. Huguenin, Spin-orbit X states, *Phys. Rev. A* **103**, 022411 (2021).
- [43] D. G. Braga, I. Fonseca, W. F. Balthazar, M. S. Sarandy, and J. A. O. Huguenin, Spin-orbit maximally discordant mixed states, *Phys. Rev. A* **106**, 062403 (2022).
- [44] V. S. Lamego, D. G. Braga, L. S. Oliveira, W. F. Balthazar, and J. A. O. Huguenin, Partial nonseparability of spin-orbit modes, *J. Opt.* **25**, 034001 (2023).
- [45] S. Pirandola, Quantum discord as a resource for quantum cryptography, *Sci. Rep.* **4**, 6956 (2014).
- [46] A. Brodutch *et al.*, Quantum discord in quantum computation, *J. Phys.: Conf. Ser.* **306**, 012030, (2011).
- [47] G. Adesso, M. Cianciaruso, and T. R. Bromley, An introduction to quantum discord and non-classical correlations beyond entanglement, [arXiv:1611.01959](https://arxiv.org/abs/1611.01959).
- [48] A. Bera *et al.*, Quantum discord and its allies: A review of recent progress, *Rep. Prog. Phys.* **81**, 024001 (2018).
- [49] S. Virzi *et al.*, Optimal estimation of entanglement and discord in two-qubit states, *Sci. Rep.* **9**, 3030 (2019).
- [50] C. Benedetti *et al.*, Experimental estimation of quantum discord for a polarization qubit and the use of fidelity to assess quantum correlations, *Phys. Rev. A* **87**, 052136 (2013).
- [51] J. B. Altepeter, E. R. Jeffrey, and P. G. Kwiat, Photonic state tomography, *Adv. At. Mol. Opt. Phys.* **52**, 105 (2005).